
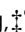










## EDGE ARTICLE

Cite this: *Chem. Sci.*, 2021, 12, 702

All publication charges for this article have been paid for by the Royal Society of Chemistry

## Aggregation-induced phosphorescence sensitization in two heptanuclear and decanuclear gold–silver sandwich clusters†

Zhou Lu,  ‡<sup>ab</sup> Yu-Jie Yang,  ‡<sup>c</sup> Wen-Xiu Ni,  <sup>d</sup> Mian Li,  <sup>c</sup> Yifang Zhao,  <sup>a</sup>  
Yong-Liang Huang,  <sup>d</sup> Dong Luo,  <sup>a</sup> Xiaoping Wang,  <sup>e</sup>  
Mohammad A. Omary  <sup>\*b</sup> and Dan Li  <sup>\*a</sup>

The strategy of aggregation-induced emission enhancement (AIEE) has been proven to be efficient in wide areas and has recently been adopted in the field of metal nanoclusters. However, the relationship between atomically precise clusters and AIEE is still unclear. Herein, we have successfully obtained two few-atom heterometallic gold–silver hepta-/decanuclear clusters, denoted  $\text{Au}_6\text{Ag}$  and  $\text{Au}_9\text{Ag}$ , and determined their structures by X-ray diffraction and mass spectrometry. The nature of the  $\text{Au}^{\text{I}}\cdots\text{Ag}^{\text{I}}$  interactions thereof is demonstrated through energy decomposition analysis to be far-beyond typical closed-shell metal–metal interaction dominated by dispersion interaction. Furthermore, a positive correlation has been established between the particle size of the nanoaggregates and the photoluminescence quantum yield for  $\text{Au}_6\text{Ag}$ , manifesting AIEE control upon varying the stoichiometric ratio of Au : Ag in atomically-precise clusters.

Received 15th September 2020

Accepted 29th October 2020

DOI: 10.1039/d0sc05095d

rsc.li/chemical-science

## Introduction

Synthesis of few-atom nanoclusters (NCs) is a work of art and represents the atomic precision of chemistry, building a bridge from traditional coordination chemistry to plasmonic metal clusters.<sup>1–5</sup> With advanced single crystal X-ray analysis and high-quality mass spectrometry techniques at hand, precise formulas and total structures of both cluster kernels and protecting ligands can be obtained to facilitate the exploration of the structure–property relationship at the molecular scale.<sup>6,7</sup> Nevertheless, achieving a unanimous interpretation of metal–metal interaction (aka. metal–metal interaction) in fields spanning from oligomeric metal complexes to atomically precise metal

NCs remains a Sisyphus task by means of multiple descriptions in different narratives.<sup>1,2,8–18</sup>

So far, the majority of research studies in these fields have focused on same-atom clusters rather than heterometallic ones due to the synthetic challenge of controllable doping/tailoring of another kind of atom at the level of atomic precision.<sup>5,7,14,19</sup> One of the topical studies is the doping of silver atoms into gold clusters, whereby their same valence shell electrons and similar coordination modes could bring unique optoelectronic behaviours.<sup>20–26</sup> A representative example is gradually substituting gold atoms with silver in the 25-metal-atom NC  $\text{Ag}_x\text{Au}_{25-x}$  and the 13th silver atom replacement results in a 200-fold boost in photoluminescence quantum yield ( $\Phi_{\text{PL}}$ )<sup>20</sup> which is attributed to a combination of stabilization of the lowest unoccupied molecular orbital (LUMO), rigidity enhancement, and symmetry preservation despite the great perturbation of the electronic structure.<sup>21</sup> In other words, the stoichiometric ratio of Au : Ag is a key factor in regulating the photophysics of these molecular clusters.<sup>22–26</sup>

The aggregation of molecules in solution is a ubiquitous phenomenon in supramolecular and biological systems and has been recognized as a promising strategy to enhance the photoluminescence of ordered nanostructures by virtue of metal–metal interactions/bondings,<sup>27–30</sup> sometimes accompanied by other non-covalent interactions among the protecting ligands (e.g.  $\pi$ – $\pi$ /C–H $\cdots$  $\pi$  interactions, hydrogen bonding).<sup>31</sup> The concept of aggregation-induced emission (AIE), first discovered in a class of organic molecules undergoing a mechanism of restriction of intramolecular motions (RIM) to boost luminescence,<sup>32</sup> is now relegated to a phenomenal description

<sup>a</sup>College of Chemistry and Materials Science, Guangdong Provincial Key Laboratory of Functional Supramolecular Coordination Materials and Applications, Jinan University, Guangzhou 510632, P. R. China. E-mail: danli@jnu.edu.cn

<sup>b</sup>Department of Chemistry, University of North Texas, 1155 Union Circle #305070, Denton, Texas 76203, USA. E-mail: omary@unt.edu

<sup>c</sup>Department of Chemistry, Shantou University, Guangdong 515063, P. R. China

<sup>d</sup>Department of Chemistry, Shantou University Medical College, Shantou, Guangdong 515041, P. R. China

<sup>e</sup>Neutron Scattering Division, Oak Ridge National Laboratory, Oak Ridge, Tennessee 37831-6475, USA

† Electronic supplementary information (ESI) available: General synthesis, characterizations, crystallography studies, photoluminescence data, computational details and results. CCDC 1968678 and 1968679. For ESI and crystallographic data in CIF or other electronic format see DOI: 10.1039/d0sc05095d

‡ Z. L. and Y.-J. Y. contributed to this work equally.



propagating broadly to many areas, such as metal complexes,<sup>33,34</sup> supramolecular cages<sup>35,36</sup> and self-assembled metal NCs.<sup>27,37–44</sup> It is unsurprising that a mist steals over the comprehension of AIE in NCs given the deadlock of even more blurred structure–property correlation compared with the aforementioned.

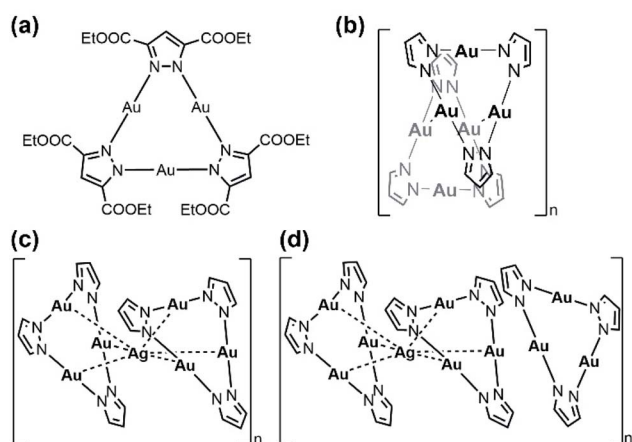
Previously, we have demonstrated the self-assembly of a cyclic trinuclear Au<sup>I</sup>–pyrazolate complex and silver cation in solution or by mechanochemistry approaches and managed to determine the single crystallographic structure of a heptanuclear sandwich-like cluster.<sup>45</sup> Herein, we report the synthesis, crystal structure, metal–metal bonding analyses, and unusual observation of stoichiometric-ratio-dependent aggregation-induced emission enhancement (AIEE) in the self-assembly processes of two atomically precise gold–silver clusters in solution.

## Results and discussion

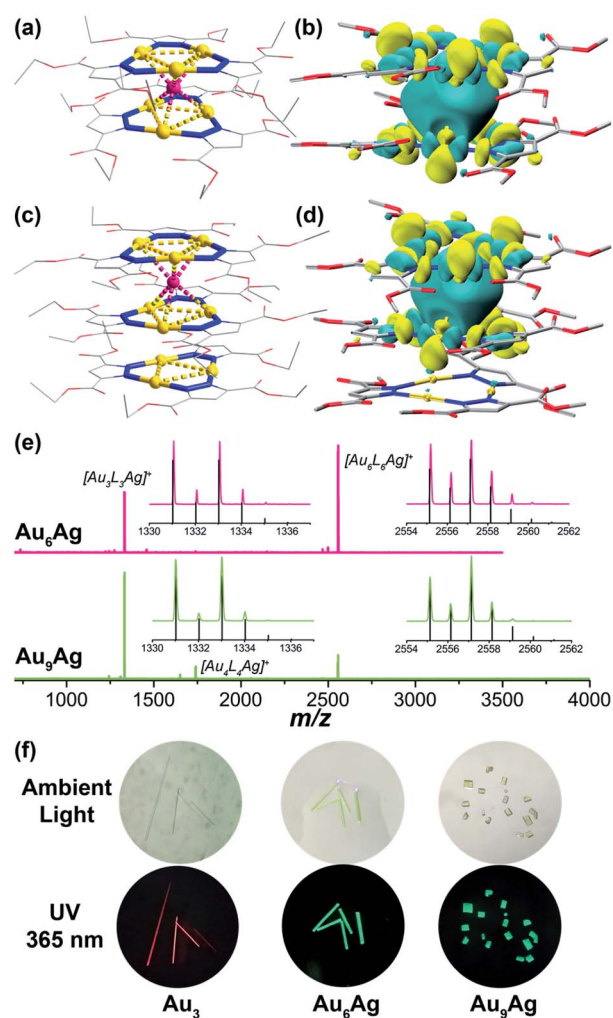
The cyclic trinuclear Au<sup>I</sup> complex (denoted **Au<sub>3</sub>**, Scheme 1a) based on the ligand bis-3,5-(ethoxycarbonyl)<sub>2</sub>-1H-pyrazole (*HL*) was chosen as the precursor due to its unique near-planar geometry and aromatic/electron-rich property.<sup>1,2,46</sup> In previous work done by Chilukuri, Omary, Hipps, and co-workers, **Au<sub>3</sub>** showed one-dimensional chair-stacking led by two pairs of alternate intermolecular Au<sup>I</sup>⋯Au<sup>I</sup> interactions (Scheme 1b, 3.273 Å & 3.493 Å).<sup>47</sup> The reported routes to heterometallic NCs include co-reduction of two metal ion precursors, intercluster reactions and metal tailoring to homometallic NCs, which lack the prediction of the doping/alloying positions. Controllable syntheses at a precise atomic level have been occasionally reported by adopting a metal cluster as the precursor owing to abundant metal/ligand interacting sites, especially through the insertion of a silver cation into Au NCs.<sup>14,48</sup> In the present work, solution-based reactions between **Au<sub>3</sub>** and AgPF<sub>6</sub> in different stoichiometric ratios afford two sandwich-like clusters [**Au<sub>3</sub>**–

Ag<sup>+</sup>–**Au<sub>3</sub>**][PF<sub>6</sub><sup>–</sup>] and {**Au<sub>3</sub>**–Ag<sup>+</sup>–[**Au<sub>3</sub>**]<sub>2</sub>}[PF<sub>6</sub><sup>–</sup>] (denoted **Au<sub>6</sub>Ag** and **Au<sub>9</sub>Ag**, Scheme 1c and d) supported by Lewis-acid/π-base and cation–π interactions, restricting foreign ions along the C<sub>3</sub> axis (Fig. 1).

X-ray photoelectron spectroscopy (XPS) studies proved the monovalence of the gold and silver atoms without reduction before or after the reactions (Fig. S5†). Single crystals suitable for X-ray structural analysis were obtained from gas-phase diffusion or slow evaporation under room temperature for needle-like **Au<sub>6</sub>Ag** and block-shaped **Au<sub>9</sub>Ag**, respectively. X-ray crystallographic studies reveal that both heterometallic Au<sup>I</sup>–Ag<sup>I</sup> clusters exhibit infinite column stacking modes in one dimension (*c*-axis), containing sandwich-like [**Au<sub>3</sub>**–Ag<sup>+</sup>–**Au<sub>3</sub>**] fragments (Fig. 1a, c and S13–S15†). **Au<sub>6</sub>Ag** crystallizes in a *P6̄* space group and **Au<sub>9</sub>Ag** crystallizes in a *P62c* space group; **Au<sub>3</sub>**



**Scheme 1** Chemical structures of (a) **Au<sub>3</sub>** and (b) a dimer of **Au<sub>3</sub>**, and sandwich complexes (c) **Au<sub>6</sub>Ag** and (d) **Au<sub>9</sub>Ag** discussed in this work (ligand substituents and counteranions PF<sub>6</sub><sup>–</sup> are omitted from the figures for clarity).



**Fig. 1** Crystal structures for (a) **Au<sub>6</sub>Ag** and (c) **Au<sub>9</sub>Ag** and molecular orbital contours of the LUMOs for (b) **Au<sub>6</sub>Ag**\* and (d) **Au<sub>9</sub>Ag**\* (*vide infra*, isovalue = 0.02). Hydrogens, counteranions PF<sub>6</sub><sup>–</sup>, and disordered sets in the **Au<sub>3</sub>** rings and Ag cations are omitted from the figures for clarity. (e) MALDI-TOF-MS spectra of (top) **Au<sub>6</sub>Ag** and (bottom) **Au<sub>9</sub>Ag**. Inset: simulated and measured isotopic distributions of (left) [**Au<sub>3</sub>L<sub>3</sub>Ag**]<sup>+</sup> and (right) [**Au<sub>6</sub>L<sub>6</sub>Ag**]<sup>+</sup> fragments. (f) Digital photographs of crystals of **Au<sub>3</sub>**, **Au<sub>6</sub>Ag** and **Au<sub>9</sub>Ag** under ambient and 365 nm UV light, respectively.

species remain intact in both heterobimetallic clusters and follow the  $C_3$  rotation symmetry. Different from other ligand-unsupported Au–Ag clusters, the sole silver cation is totally surrounded by six Au atoms (not coordinated with organic ligands) to form a twisted trigonal prism; the distances of the Au–Ag contacts fall in the range of 2.617(5)–2.7871(7) Å (Table S2†), shorter than most ligand-supported/unsupported gold–silver contacts.<sup>49</sup> Besides, in **Au<sub>6</sub>Ag**, we also find an additional **Au<sub>3</sub>** in the repeating unit showing close intertrimer Au⋯Au distances of 3.175(6)–3.649(3) Å (Fig. 1c). The full-sandwich-like fragments ( $[\text{Au}_6\text{L}_6\text{Ag}]^+$ ,  $m/z = 2557.198$  in **Au<sub>6</sub>Ag**; 2557.138 in **Au<sub>6</sub>Ag**) and half-sandwich fragments ( $[\text{Au}_3\text{L}_3\text{Ag}]^+$ ,  $m/z = 1333.060$  in **Au<sub>6</sub>Ag**; 1333.009 in **Au<sub>6</sub>Ag**), as well as their resolved isotopic peaks, are confirmed by matrix-assisted laser desorption/ionization time-of-flight mass spectroscopy (MALDI-TOF-MS, Fig. 1e). The full triple-decker cluster of **Au<sub>9</sub>Ag** ( $[\text{Au}_9\text{L}_9\text{Ag}]^+$ , calculated  $m/z = 3781.253$ ) could not be observed in the MS study, probably due to the lability of the intermolecular  $\text{Au}^{\text{I}}\cdots\text{Au}^{\text{I}}$  interactions.

To evaluate the binding energies of ligand-unsupported  $\text{Au}^{\text{I}}\cdots\text{Ag}^{\text{I}}$  and  $\text{Au}^{\text{I}}\cdots\text{Au}^{\text{I}}$  interactions, density functional theory (DFT) calculations were carried out (ESI† Computational section). In previous reports, the estimated energy of 14 kcal mol<sup>−1</sup> was regarded as ligand-unsupported  $\text{Au}^{\text{I}}\cdots\text{Ag}^{\text{I}}$  metalphilicity and ground state charge-transfer character, behaving like “loose clusters”.<sup>9</sup> Here, our energy decomposition analysis (EDA) reveals that electrostatic attraction and orbital interaction also make considerable contributions, suggesting that the interaction between the silver cations and **Au<sub>3</sub>** is beyond Lewis acid/ $\pi$ -base or cation– $\pi$  interactions (Fig. S28†). The orbital interaction value of  $\sim 18$  kcal mol<sup>−1</sup> for each ligand-unsupported  $\text{Au}^{\text{I}}\cdots\text{Ag}^{\text{I}}$  interaction (six pairs of  $\sim 110$  kcal mol<sup>−1</sup> in total, Table S9†) is regarded as strong (dative) bonding by the natural orbitals for chemical valence (NOCV) method with electron-sharing from gold to silver, along with considerable dispersion energy (Fig. S29–S33†).<sup>8,18,50,51</sup> A recent report revealed that for metal–metal bonds of metals with filled d-orbitals, the charge-shift character increases as the covalency decreases.<sup>52</sup> The electrostatic interactions lead to contributions of about 50% to the attraction energies in the EDA results, corresponding to the remarkable charge-shift character of the later transition metals. As a result, the synergic non-bonding interactions, including Lewis acid/ $\pi$ -base interactions (electrostatic derivation) and closed-shell metal–metal interactions (dispersion force), lead to Au–Ag bonding (orbital interactions) with remarkable bonding energies. Besides, the intertrimer  $\text{Au}^{\text{I}}\cdots\text{Au}^{\text{I}}$  interactions in **Au<sub>9</sub>Ag** are only reckoned as aurophilicity-mediated by relativistic effects, reflected by the other derivative dispersion energy.<sup>53</sup> According to the molecular orbital analysis, the LUMOs of **Au<sub>6</sub>Ag**\* and **Au<sub>9</sub>Ag**\* (replacing ethoxycarbonyl with methoxycarbonyl groups due to little contribution to the electronic structures) are mainly composed of the Au 5d and Ag 5s atomic orbitals in the sandwich-like fragments (Fig. 1b and d), showing strong sd hybridizations attributed to relativistic contractions.<sup>7,20,54</sup> The inserted silver cation only alters the electronic density of the sandwich-like fragments in **Au<sub>6</sub>Ag**\*, with the additional **Au<sub>3</sub>** hardly

contributing to the LUMO.<sup>45</sup> By contrast, the composition of the 5d<sub>z<sup>2</sup></sub> orbitals from all Au atoms could be identified in doubly-degenerate filled frontier orbitals (two highest-occupied molecular orbitals (HOMOs) and two next-HOMOs (HOMO–1s) – see Fig. S36–S37†). This indicates remarkable metal contribution to the frontier occupied molecular orbitals. The energy level diagram (Scheme S1†) clearly reflects the great perturbation of the inserted silver ions, rendering higher-density electron delocalization in the metal kernels, as well as more stabilized frontier virtual orbitals (LUMOs) and narrower HOMO–LUMO gaps.

**Au<sub>3</sub>**, **Au<sub>6</sub>Ag**, and **Au<sub>9</sub>Ag** are all strongly emissive in the solid state (Fig. 1f and S16†). The homometallic **Au<sub>3</sub>** emits at the maximum of 670 nm with  $\Phi_{\text{PL}}$  of 67.5% under room temperature; both heterobimetallic nanoclusters **Au<sub>6</sub>Ag** and **Au<sub>9</sub>Ag** show the maximum emission peak at 496 nm with  $\Phi_{\text{PL}}$  of 43.9% and 12.0%, respectively. The room-temperature emission lifetimes fall into the microsecond region ( $\tau = 15.32, 9.31, \text{ and } 9.11 \mu\text{s}$  for **Au<sub>3</sub>**, **Au<sub>6</sub>Ag**, and **Au<sub>9</sub>Ag**, respectively; Table S5, Fig. S25 and S26†), characteristic of phosphorescence. Time-dependent density functional theory (TD-DFT) calculations reveal that the phosphorescence of **Au<sub>3</sub>** originates from intra-ligand charge transfer (<sup>3</sup>ILCT) and metal-to-ligand charge transfer (<sup>3</sup>MLCT), despite the relatively short intermolecular Au⋯Au distances. In contrast, the added  $\text{Au}^{\text{I}}\cdots\text{Ag}^{\text{I}}$  bonding manifests as low-energy absorption (around 400 nm, Fig. S17†), consistent with the TD-DFT results of ligand-protected metal centred (<sup>1</sup>MC/<sup>3</sup>MC) characteristics (Fig. S28 and Tables S14–S17†).

All of these homometallic and heterometallic clusters show good solubility in dichloromethane solution and are still strongly emissive. Unlike common phosphorescent complexes/clusters,<sup>55–57</sup> it is exciting that these NCs are insensitive to oxygen quenching due to ligand-protected metal cores (Table S8†). **Au<sub>3</sub>** exhibits a high-energy absorption peak at 264 nm and two distinct emission peaks at around 350 and 710 nm in

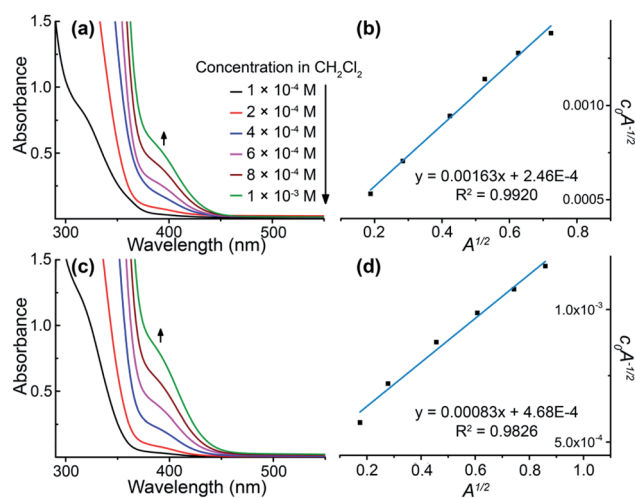


Fig. 2 Varied-concentration UV-vis absorption spectra for (a) **Au<sub>6</sub>Ag** and (c) **Au<sub>9</sub>Ag**. Plots of  $c_0 A^{-1/2}$  versus  $A^{1/2}$  taken at the respective low-energy absorption bands (392 and 394 nm), characteristic of dimers of (b) **Au<sub>6</sub>Ag** and (d) **Au<sub>9</sub>Ag**.



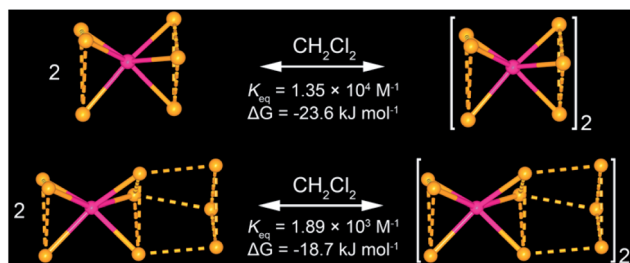


Chart 1 Illustrations of monomer–dimer aggregation in  $\text{CH}_2\text{Cl}_2$  solution of (top)  $\text{Au}_6\text{Ag}$  from heptanuclear to tetradecanuclear clusters and (bottom)  $\text{Au}_9\text{Ag}$  from decanuclear to icosanuclear clusters. Only gold and silver atoms, and one set of disordered atoms, are presented for clarity purposes.

$\text{CH}_2\text{Cl}_2$  solution (Fig. S22<sup>†</sup>), which fall into the near UV and infrared regions. As shown in Fig. 2a and c, both  $\text{Au}_6\text{Ag}$  and  $\text{Au}_9\text{Ag}$  exhibit a high-energy monomer absorbance peak at around 315 nm and an additional low-energy oligomer band at around 390 nm at higher concentrations. By calculations of apparent molar extinction coefficients, deviation from Beer's law is observed for the lower-energy absorption bands around 390 nm, as depicted and analysed in Fig. 2b, d, and S21,<sup>†</sup> respectively.<sup>58</sup> Further analyses and good linearities confirm the assumption of monomer–dimer aggregations of both  $\text{Au}_6\text{Ag}$  and  $\text{Au}_9\text{Ag}$  in  $\text{CH}_2\text{Cl}_2$  solution, giving rise to remarkable nano-scale clustering into an  $[\text{Au}_6\text{Ag}]_2$  tetradecanuclear 14-metal-atom cluster and an  $[\text{Au}_9\text{Ag}]_2$  icosanuclear 20-metal-atom cluster—giving rise to respective equilibrium constants ( $K_{\text{eq}}$ ) of *ca.*  $1.35 \times 10^4 \text{ M}^{-1}$  and  $1.89 \times 10^3 \text{ M}^{-1}$ , and Gibbs free energy ( $\Delta G$ ) of  $-23.6$  and  $-18.7 \text{ kJ mol}^{-1}$  at 298 K (Table S6<sup>†</sup> and Chart 1).

Solution-state photoluminescence measurements were also conducted for both heterobimetallic clusters and only  $\text{Au}_6\text{Ag}$  shows a dependent correlation between the luminescence efficiency and concentration (Fig. 3a). Similar to the absorption spectra, a consistent trend of excitation energy *versus* concentration is also observed for both  $\text{Au}_6\text{Ag}$  and  $\text{Au}_9\text{Ag}$  (Fig. 3b and c), showing intensity increment of the low-energy band and bathochromic shift of the high-energy band, which finally combine into a broad excitation band at high concentrations.<sup>45</sup> Moreover, the positive correlations between the luminescence intensity and concentrations of these two clusters are also verified. Different from the absorption and excitation, no spectral shift, but increased emission intensities, are observed when concentrating the gold–silver clusters in solution, both showing maxima at 491 nm (Fig. 3d and e), almost identical to that of solid-state emissions.

A further step is to demonstrate that the gold–silver clusters have indeed undergone aggregation processes in solution and to quantify the emission enhancement, *i.e.* fully confirming the AIEE phenomenon. Dynamic light scattering (DLS) experiments clearly reveal the generation of nanoaggregates of  $\text{Au}_6\text{Ag}$  and  $\text{Au}_9\text{Ag}$  (Fig. 4a, b and Table 1), which could also be witnessed by scanning electron microscopy (Fig. 4c, d and S10<sup>†</sup>). The average particle diameter of  $\text{Au}_6\text{Ag}$  expands from 109 nm at 0.01 mM to

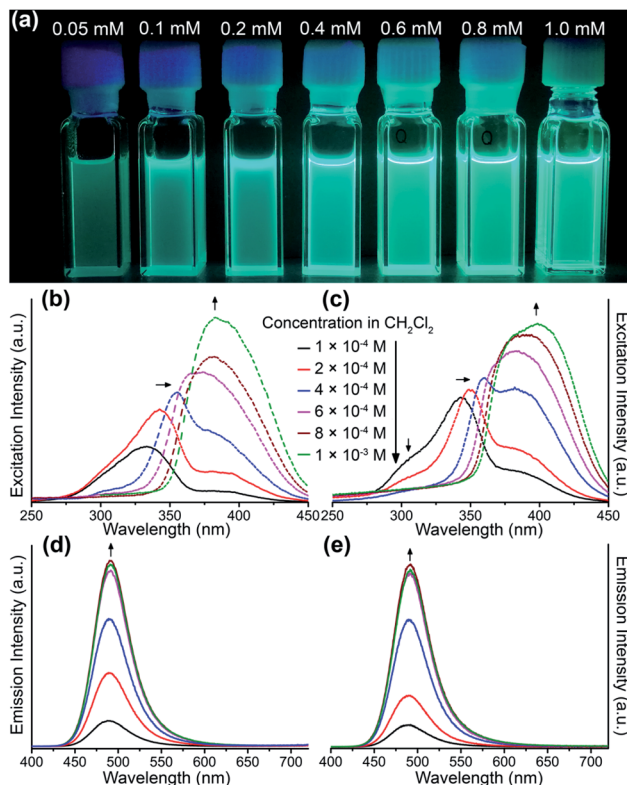


Fig. 3 (a) Digital photographs of  $\text{Au}_6\text{Ag}$  in  $\text{CH}_2\text{Cl}_2$  solution of varied concentrations under 365 nm UV light. Varied-concentration excitation and emission spectra for (left: b and d)  $\text{Au}_6\text{Ag}$  and (right: c and e)  $\text{Au}_9\text{Ag}$  in  $\text{CH}_2\text{Cl}_2$  solution under room temperature, respectively. The excitation wavelengths were 300 nm and the monitored emission wavelengths were 490 nm.

471 nm at 1.0 mM, while that of  $\text{Au}_9\text{Ag}$  remains at around 150 nm in the range of 0.1 mM and 1.0 mM. As shown in Table 1, the size of the nanoaggregates directly influences the  $\Phi_{\text{PL}}$

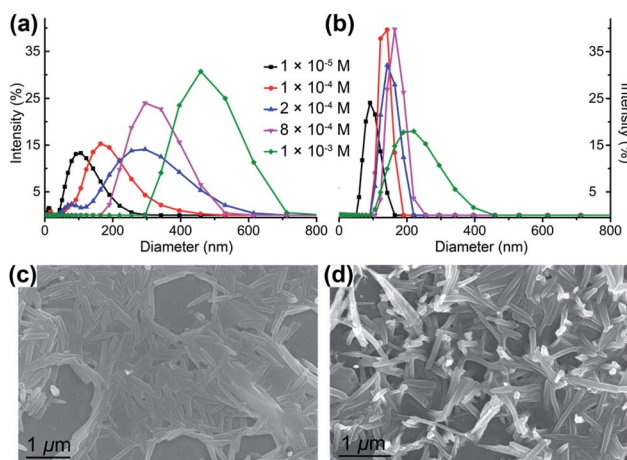


Fig. 4 Dynamic light scattering (DLS) results for (a)  $\text{Au}_6\text{Ag}$  and (b)  $\text{Au}_9\text{Ag}$  characterizing the size distributions of the nanoaggregates in  $\text{CH}_2\text{Cl}_2$  solution of different concentrations. Scanning electron microscope (SEM) images prepared from the 1.0 mM  $\text{CH}_2\text{Cl}_2$  solution of (c)  $\text{Au}_6\text{Ag}$  and (d)  $\text{Au}_9\text{Ag}$ .

**Table 1** Correlation of the concentrations of the clusters, sizes of the nanoaggregates and absolute  $\Phi_{\text{PL}}$  for  $\text{Au}_6\text{Ag}$  and  $\text{Au}_9\text{Ag}$  in  $\text{CH}_2\text{Cl}_2$  solution

Cluster	Concentration [mM]	Average particle diameter [nm]	$\Phi_{\text{PL}}$ [%]
$\text{Au}_6\text{Ag}$	0.1	179	27.0
	0.2	283	31.6
	0.4	—	42.8
	0.6	—	51.8
	0.8	316	50.2
	1.0	471	60.6
$\text{Au}_9\text{Ag}$	0.1	134	34.0
	0.2	148	36.4
	0.4	—	40.9
	0.6	—	36.4
	0.8	166	39.5
	1.0	216	34.2

magnitudes, which range from  $\Phi_{\text{PL}}$  of 27.0% to 60.6% for an average diameter of 179 nm to 471 nm, respectively, for  $\text{Au}_6\text{Ag}$ . In contrast,  $\text{Au}_9\text{Ag}$  exhibits steady  $\Phi_{\text{PL}}$  values of around 37% and particle diameters of around 150 nm. It is interesting to observe such an unusual stoichiometric-ratio-dependent AIEE behaviour in a system of atomically precise clusters.

A helpful insight to justify the  $\Phi_{\text{PL}}$ /AIEE trend variation in the hepta- vs. deca-nuclear clusters herein is provided by the calculated radiative/non-radiative decay rate constants ( $\text{Au}_6\text{Ag}$ :  $1.69/4.59 \times 10^4 \text{ s}^{-1}$  at 0.1 mM,  $3.19/2.07 \times 10^4 \text{ s}^{-1}$  at 1.0 mM;  $\text{Au}_9\text{Ag}$ :  $2.05/3.98 \times 10^4 \text{ s}^{-1}$  at 0.1 mM,  $1.94/3.74 \times 10^4 \text{ s}^{-1}$  at 1.0 mM). For  $\text{Au}_6\text{Ag}$ , the inhibition of non-radiative decay upon aggregation is in line with the phenomenal description of AIE,<sup>32</sup> but the promotion of the radiative transition efficiency is unconventional. Comparing the crystallographic disorder in the columnar structures of  $\text{Au}_6\text{Ag}$  and  $\text{Au}_9\text{Ag}$  (Fig. S14 and S15<sup>†</sup>), one might notice that the silver cations in the former experience partial occupancy disorder along the  $C_3$  axis. In the literature, weakly-disordered systems with reduced effective mass were suggested to have strong electron/hole mobility that is responsible for the enhanced photoluminescence.<sup>20,59</sup> Besides, *via* quantitative analysis of solution-state absorption spectra, we have attained a  $7\times$  larger equilibrium constant ( $K_{\text{eq}}$ ) for  $\text{Au}_6\text{Ag}$  than for  $\text{Au}_9\text{Ag}$ , suggesting a stronger tendency for the former to aggregate in solution (Table S6<sup>†</sup> and Chart 1).

## Conclusions

Herein, different narratives for ligand-unsupported  $d^{10}$ - $d^{10}$   $M-M'$  interactions (with covalent bonding strength) and aggregation-induced emission enhancement (with larger than doubled  $\Phi_{\text{PL}}$ ) are provided for sandwich-like gold-silver clusters through a combined experimental/computational study. The synergy effect, from Lewis acid/ $\pi$ -base interactions and metal-metal interactions (metallophilicity), gives rise to enhanced stability of the sandwich-like structures with ligand-unsupported Au-Ag bonding interactions and the comprehension of the bonding nature between  $d^{10}$  metals. The regulation of the stoichiometric ratio of Au : Ag in the nanoclusters with

similar morphology results in nanocluster aggregation and further emission enhancement. Thus, a bridge is built between the effect of doping a foreign silver ion into cyclic trinuclear  $\text{Au}^{\text{I}}$  complexes and the photophysical properties regulated by the Au : Ag ratio in the aggregated nanoclusters.

## Experimental section

### Materials

All starting materials were purchased from commercial sources and used as received without further purification. The solvents used for synthesis were of analytical grade and those for the photophysical studies were of HPLC grade. Detailed characterization methods are included in the ESI.<sup>†</sup>

### Synthesis of cyclo-trimer gold(i) bis-3,5-(ethoxycarbonyl)-pyrazolate $\text{Au}_3$

To 15 mL of an ethanol solution of bis-3,5-(ethoxycarbonyl)-1*H*-pyrazole (*HL*, 0.106 g, 0.5 mmol), 30 mL of an acetone solution of gold(tetrahydrothiophene)chloride (0.160 g, 0.5 mmol) was added. After the addition of a few drops of anhydrous triethylamine, a white precipitate immediately formed and the suspension was stirred for another 15 min to react completely. The white precipitate was collected by filtration and washed with methanol, acetone, and diethyl ether ( $3 \times 1 \text{ mL}$  for each) in a high yield (0.165 g, yield 82%) showing bright red emission under UV light. UV-vis in  $\text{CH}_2\text{Cl}_2$  ( $\lambda_{\text{max}}/\text{nm}$ ): 264. FT-IR (KBr pellet,  $\nu/\text{cm}^{-1}$ ): 3169w, 2984w, 1735s, 1465m, 1433m, 1387m, 1370m, 1257s, 1180s, 1089m, 1039m, 1018w, 848s, 759m, 628w. Elemental analyses for  $\text{Au}_3\text{C}_{27}\text{O}_{12}\text{N}_6\text{H}_{33}$ , found: C, 26.82; H, 2.929; N, 6.75; calcd: C, 26.48; H, 2.716; N, 6.86.  $^1\text{H-NMR}$  ( $\text{CDCl}_3$ , 400 MHz):  $\delta/\text{ppm} = 7.60$  (s, 2.7, -pyrazolate), 4.45 (q, 12.0,  $-\text{CH}_2-$ ), 1.40 (t, 18.5,  $-\text{CH}_3$ ).

### Synthesis of $[\text{Au}_3\text{-Ag-Au}_3][\text{PF}_6]$ ( $\text{Au}_6\text{Ag}$ )

A mixture of  $\text{AgPF}_6$  (0.008 g, 0.03 mmol) and two equivalents of  $\text{Au}_3$  (0.077 g, 0.06 mmol) in 10 mL of  $\text{CH}_2\text{Cl}_2$  solution was stirred under room temperature for 30 min to afford a greenish suspension. Needle-like crystals of  $[\text{Au}_3\text{-Ag-Au}_3][\text{PF}_6]$  (denoted as  $\text{Au}_6\text{Ag}$ ) were obtained by diffusing *n*-hexane/diethylether (3 : 2, v/v) into the greenish transparent filtrate (0.068 g, yield 80%). MALDI-TOF-MS ( $\alpha$ -cyano-4-hydroxycinnamic acid as the matrix):  $m/z$  for  $[\text{Au}_3\text{L}_3\text{Ag}]^+$ : found 1333.060, calcd 1333.020;  $[\text{Au}_6\text{L}_6\text{Ag}]^+$ : found 2557.198, calcd 2557.134. FT-IR (KBr pellet,  $\nu/\text{cm}^{-1}$ ): 3169w, 2984m, 1128s, 1710s, 1531m, 1470m, 1428w, 1389w, 1369m, 1308m, 1271s, 1255s, 1230s, 1178s, 1080s, 1038m, 1018w, 852m, 762s, 628w. Elemental analyses for  $\text{Au}_6\text{C}_{54}\text{O}_{24}\text{N}_{12}\text{H}_{66}\text{AgPF}_6$ , found: C, 24.33; H, 2.305; N, 6.35. Calcd: C, 24.01; H, 2.462; N, 6.22.  $^1\text{H-NMR}$  ( $\text{CDCl}_3 + \text{CH}_2\text{Cl}_2$ , 500 MHz):  $\delta/\text{ppm} = 6.68$  (br, 6.2, -pyrazolate), 4.04 (br, 24.0,  $-\text{CH}_2-$ ), 1.21 (br, 36.8,  $-\text{CH}_3$ ).

### Synthesis of $\{[\text{Au}_3]_2\text{-Ag-Au}_3\}[\text{PF}_6]$ ( $\text{Au}_9\text{Ag}$ )

A mixture of  $\text{AgPF}_6$  (0.008 g, 0.03 mmol) and more than three equivalents of  $\text{Au}_3$  (0.123 g, 0.10 mmol) in 10 mL of  $\text{CH}_2\text{Cl}_2$  solution was stirred under room temperature for 30 min to

afford a greenish suspension. After evaporating off the greenish filtrate under room temperature, block-shaped crystals along with a black solid could be found in the vial. A mixed solvent of ethyl acetate and  $\text{CH}_2\text{Cl}_2$  (1 : 10, v/v) was used to dissolve the crystals and insoluble substances were filtered out. Block-shaped crystals of  $\{[\text{Au}_3]_2\text{-Ag-Au}_3\}[\text{PF}_6]$  (denoted as **Au<sub>9</sub>Ag**) were obtained by evaporating the greenish transparent ethyl acetate/ $\text{CH}_2\text{Cl}_2$  filtrate under room temperature (0.056 g, yield 47%). MALDI-TOF-MS ( $\alpha$ -cyano-4-hydroxycinnamic acid as the matrix):  $m/z$  for  $[\text{Au}_3\text{L}_3\text{Ag}]^+$ , found 1333.009, calcd 1333.020;  $[\text{Au}_4\text{L}_4\text{Ag}]^+$ , found 1741.057, calcd 1741.059;  $[\text{Au}_6\text{L}_6\text{Ag}]^+$ : found 2557.138, calcd 2557.134. FT-IR (KBr pellet,  $\nu/\text{cm}^{-1}$ ): 2982m, 1740s, 1716s, 1635w, 1526w, 1472m, 1435m, 1386m, 1368m, 1254s, 1174s, 1082m, 1038m, 843s, 757m, 626w, 558w. Elemental analyses for  $\text{Au}_9\text{C}_{81}\text{O}_{36}\text{N}_{18}\text{H}_{99}\text{AgPF}_6$ , found: C, 24.96; H, 2.578; N, 6.53. Calcd: C, 24.78; H, 2.541; N, 6.42.  $^1\text{H-NMR}$  ( $\text{CDCl}_3 + \text{CH}_2\text{Cl}_2$ , 500 MHz):  $\delta/\text{ppm} = 7.44$  (br, 10.9, -pyrazolate), 4.40 (br, 36.0,  $-\text{CH}_2-$ ), 1.39 (t, 52.4,  $-\text{CH}_3$ ).

### Crystallographic study

X-ray crystallographic data were collected on a XtaLab PRO MM007HF DW Diffractometer System equipped with a MicroMax-007DW MicroFocus X-ray generator and Pilatus 200K silicon disarray detector (Rigaku, Japan, Cu  $K\alpha$ ,  $\lambda = 1.54184 \text{ \AA}$  or Mo  $K\alpha$ ,  $\lambda = 0.71073 \text{ \AA}$ ) under 293 K or 100 K. Data reductions were performed on CrysAlisPro. Structures were solved by using direct methods by ShelXT for **Au<sub>3</sub>** and SIR2004 for **Au<sub>9</sub>Ag** in the OLEX2 program package, and all non-hydrogen atoms were refined anisotropically by the full-matrix least-squares method on  $F^2$  by using the ShelXL program.<sup>60</sup> The hydrogen atoms were located from different maps and refined with isotropic temperature factors. In the **Au<sub>9</sub>Ag** structure, Au and Ag atoms exhibit positional disorder. Detailed structure refined information is appended in the CIF file.

For **Au<sub>6</sub>Ag**, a fully-satisfactory crystal structure of the sample could not be obtained *via* single-crystal XRD (SCXRD) directly due to the single crystal batch's weak diffraction and the disorder problem of the ligands. The cell parameters and heavy atomic positions (Au and Ag) were generated from SCXRD data *via* the Patterson method; ligands were built based on the structure of **Au<sub>3</sub>** and refined by Rietveld refinement in the Reflex module of Materials Studio (residuals:  $R_p = 12.65\%$ ,  $R_{wp} = 19.86\%$ ). The results of EDX, mass spectra, and elemental analyses could fit the model very well. The Ag atoms in **Au<sub>6</sub>Ag** are partially occupied along the  $c$  axis in the  $P6$  space group and, therefore, the repeating unit [along  $c$ ] consists of alternating  $\{3 \text{ Au}_6\text{Ag}, 1 \text{ Au}_3 \text{ and } 1 \text{ Au}_9\text{Ag}_2\}/\{1 \text{ Au}_9\text{Ag}_2, 1 \text{ Au}_3 \text{ and } 3 \text{ Au}_6\text{Ag}\}$  clusters (Fig. S13 and S14<sup>†</sup>). The silver atoms in the **Au<sub>9</sub>Ag<sub>2</sub>** cluster adopt a face-sharing octahedral geometry  $\text{Au}_3\text{-Ag}(\mu\text{-Au})_3\text{-Ag-Au}_3$ . Based on the refinement results, silver atoms except Ag1 are half-occupied and the Au–Ag distances range from 2.641(7) to 2.713(6)  $\text{\AA}$ . The DFT-computed Au–Ag distances and their reasonable agreement with the non-disordered experiment in the **Au<sub>9</sub>Ag** model should lend some credibility to the DFT-computed Au–Ag distances in the **Au<sub>6</sub>Ag** model, which only showed reasonable distances in the 2.7  $\text{\AA}$  range.

Crystal data and structure refinement parameters are summarized in Table S1.<sup>†</sup> Selected bond lengths and angles are given in Tables S2 – S4.<sup>†</sup> CCDC no. 1968678 and 1968679 for **Au<sub>3</sub>** and **Au<sub>9</sub>Ag**.

## Conflicts of interest

There are no conflicts to declare.

## Acknowledgements

This work was financially supported by the National Natural Science Foundation of China (No. 21731002, 21975104, and 21801095), the Guangdong Major Project of Basic and Applied Research (2019B030302009), the China Postdoctoral Science Foundation (2017M622894) and Jinan University. MAO acknowledges supporting aspects of his group's contributions by the Welch Foundation (Grant B-1542), U.S. National Science Foundation (CHE-1413641), and the Shenzhen/China Peacock Plan (No. 1208040050847074). We appreciate Dr Xue Li and Xue-Zhi Wang (JNU) for the help with the mass spectrometry studies, and Dr Vladimir Nesterov (UNT) for the help with the crystallography studies.

## Notes and references

- 1 J. Zheng, Z. Lu, K. Wu, G.-H. Ning and D. Li, *Chem. Rev.*, 2020, **120**, 9675–9742.
- 2 R. Galassi, M. A. Rawashdeh-Omary, H. V. R. Dias and M. A. Omary, *Comments Inorg. Chem.*, 2019, **39**, 287–348.
- 3 R. Jin, C. Zeng, M. Zhou and Y. Chen, *Chem. Rev.*, 2016, **116**, 10346–10413.
- 4 I. Chakraborty and T. Pradeep, *Chem. Rev.*, 2017, **117**, 8208–8271.
- 5 X. Kang and M. Zhu, *Chem. Soc. Rev.*, 2019, **48**, 2422–2457.
- 6 S. Hossain, Y. Niihori, L. V. Nair, B. Kumar, W. Kurashige and Y. Negishi, *Acc. Chem. Res.*, 2018, **51**, 3114–3124.
- 7 S. Wang, Q. Li, X. Kang and M. Zhu, *Acc. Chem. Res.*, 2018, **51**, 2784–2792.
- 8 P. Pykkö, N. Runeberg and F. Mendizabal, *Chem.–Eur. J.*, 1997, **3**, 1451–1457.
- 9 E. J. Fernández, C. Hardacre, A. Laguna, M. C. Lagunas, J. M. López-de-Luzuriaga, M. Monge, M. Montiel, M. E. Olmos, R. C. Puelles and E. Sánchez-Forcada, *Chem.–Eur. J.*, 2009, **15**, 6222–6233.
- 10 R. Galassi, M. M. Ghimire, B. M. Otten, S. Ricci, R. N. McDougald Jr, R. M. Almotawa, D. Alhmoud, J. F. Ivy, A.-M. M. Rawashdeh, V. N. Nesterov, E. W. Reinheimer, L. M. Daniels, A. Burini and M. A. Omary, *Proc. Natl. Acad. Sci. U. S. A.*, 2017, **114**, E5042–E5051.
- 11 S. Jin, X. Zou, L. Xiong, W. Du, S. Wang, Y. Pei and M. Zhu, *Angew. Chem., Int. Ed.*, 2018, **57**, 16768–16772.
- 12 S. Jin, S. Wang and M. Zhu, *Chem.–Asian J.*, 2019, **14**, 3222–3231.
- 13 Q. Zheng, S. Borsley, G. S. Nichol, F. Duarte and S. L. Cockroft, *Angew. Chem., Int. Ed.*, 2019, **58**, 12617–12623.



- 14 A. Ghosh, O. F. Mohammed and O. M. Bakr, *Acc. Chem. Res.*, 2018, **51**, 3094–3103.
- 15 A. Muñoz-Castro, D. MacLeod Carey and R. Arratia-Pérez, *J. Phys. Chem. A*, 2010, **114**, 666–672.
- 16 P. Ai, M. Mauro, A. A. Danopoulos, A. Muñoz-Castro and P. Braunstein, *J. Phys. Chem. C*, 2019, **123**, 915–921.
- 17 A. Muñoz-Castro, *Inorg. Chem. Front.*, 2019, **6**, 2349–2358.
- 18 Z. Lu, B. Chilukuri, C. Yang, A.-M. Rawashdeh, R. K. K. Arvapally, S. Tekarli, X. Wang, C. Cardenas, T. R. Cundari and M. A. Omary, *Chem. Sci.*, 2020, **11**, 11179–11188.
- 19 S.-K. Peng, Z. Lu, M. Xie, Y.-L. Huang, D. Luo, J.-N. Wang, X.-W. Zhu, X. Li, X.-P. Zhou and D. Li, *Chem. Commun.*, 2020, **56**, 4789–4792.
- 20 S. Wang, X. Meng, A. Das, T. Li, Y. Song, T. Cao, X. Zhu, M. Zhu and R. Jin, *Angew. Chem., Int. Ed.*, 2014, **53**, 2376–2380.
- 21 M. Zhou, J. Zhong, S. Wang, Q. Guo, M. Zhu, Y. Pei and A. Xia, *J. Phys. Chem. C*, 2015, **119**, 18790–18797.
- 22 X.-L. Pei, Z.-G. Jiang and Q.-M. Wang, *Angew. Chem., Int. Ed.*, 2014, **53**, 12771–12775.
- 23 G. Soldan, M. A. Aljuhani, M. S. Bootharaju, L. G. AbdulHalim, M. R. Parida, A.-H. Emwas, O. F. Mohammed and O. M. Bakr, *Angew. Chem., Int. Ed.*, 2016, **55**, 5749–5753.
- 24 Z. Lei, X.-L. Pei, Z.-J. Guan and Q.-M. Wang, *Angew. Chem., Int. Ed.*, 2017, **56**, 7117–7120.
- 25 Y. Du, Z.-J. Guan, Z.-R. Wen, Y.-M. Lin and Q.-M. Wang, *Chem.–Eur. J.*, 2018, **24**, 16029–16035.
- 26 S. Jin, W. Liu, D. Hu, X. Zou, X. Kang, W. Du, S. Chen, S. Wei, S. Wang and M. Zhu, *Chem.–Eur. J.*, 2018, **24**, 3712–3715.
- 27 X. Kang, S. Wang, Y. Song, S. Jin, G. Sun, H. Yu and M. Zhu, *Angew. Chem., Int. Ed.*, 2016, **55**, 3611–3614.
- 28 Z. Wu, Y. Du, J. Liu, Q. Yao, T. Chen, Y. Cao, H. Zhang and J. Xie, *Angew. Chem., Int. Ed.*, 2019, **58**, 8139–8144.
- 29 Z. Wang, Z. Zhu, C. Zhao, Q. Yao, X. Li, H. Liu, F. Du, X. Yuan and J. Xie, *Chem.–Asian J.*, 2019, **14**, 765–769.
- 30 Q. Li, M. Zhou, W. Y. So, J. Huang, M. Li, D. R. Kauffman, M. Cotlet, T. Higaki, L. A. Peteanu, Z. Shao and R. Jin, *J. Am. Chem. Soc.*, 2019, **141**, 5314–5325.
- 31 S. Li, X.-S. Du, B. Li, J.-Y. Wang, G.-P. Li, G.-G. Gao and S.-Q. Zang, *J. Am. Chem. Soc.*, 2018, **140**, 594–597.
- 32 J. Mei, N. L. C. Leung, R. T. K. Kwok, J. W. Y. Lam and B. Z. Tang, *Chem. Rev.*, 2015, **115**, 11718–11940.
- 33 X. Yan, H. Wang, C. E. Hauke, T. R. Cook, M. Wang, M. L. Saha, Z. Zhou, M. Zhang, X. Li, F. Huang and P. J. Stang, *J. Am. Chem. Soc.*, 2015, **137**, 15276–15286.
- 34 H.-K. Cheng, M. C.-L. Yeung and V. W.-W. Yam, *ACS Appl. Mater. Interfaces*, 2017, **9**, 36220–36228.
- 35 N. Liu, T. Lin, M. Wu, H.-K. Luo, S.-L. Huang and T. S. A. Hor, *J. Am. Chem. Soc.*, 2019, **141**, 9448–9452.
- 36 H. Li, T.-Z. Xie, Z. Liang, Y. Shen, X. Sun, Y. Yang and T. Liu, *J. Phys. Chem. C*, 2019, **123**, 23280–23286.
- 37 N. Goswami, Q. Yao, Z. Luo, J. Li, T. Chen and J. Xie, *J. Phys. Chem. Lett.*, 2016, **7**, 962–975.
- 38 X. Kang, S. Wang and M. Zhu, *Chem. Sci.*, 2018, **9**, 3062–3068.
- 39 Z. Luo, X. Yuan, Y. Yu, Q. Zhang, D. T. Leong, J. Y. Lee and J. Xie, *J. Am. Chem. Soc.*, 2012, **134**, 16662–16670.
- 40 X. Dou, X. Yuan, Y. Yu, Z. Luo, Q. Yao, D. T. Leong and J. Xie, *Nanoscale*, 2014, **6**, 157–161.
- 41 Z. Wu, J. Liu, Y. Gao, H. Liu, T. Li, H. Zou, Z. Wang, K. Zhang, Y. Wang, H. Zhang and B. Yang, *J. Am. Chem. Soc.*, 2015, **137**, 12906–12913.
- 42 M. Sugiuchi, J. Maeba, N. Okubo, M. Iwamura, K. Nozaki and K. Konishi, *J. Am. Chem. Soc.*, 2017, **139**, 17731–17734.
- 43 Z. Wu, H. Liu, T. Li, J. Liu, J. Yin, O. F. Mohammed, O. M. Bakr, Y. Liu, B. Yang and H. Zhang, *J. Am. Chem. Soc.*, 2017, **139**, 4318–4321.
- 44 X. Wei, X. Kang, S. Jin, S. Wang and M. Zhu, *CCS Chem.*, 2020, **2**, 1929–1939.
- 45 W.-X. Ni, Y.-M. Qiu, M. Li, J. Zheng, R. W.-Y. Sun, S.-Z. Zhan, S. W. Ng and D. Li, *J. Am. Chem. Soc.*, 2014, **136**, 9532–9535.
- 46 S. M. Tekarli, T. R. Cundari and M. A. Omary, *J. Am. Chem. Soc.*, 2008, **130**, 1669–1675.
- 47 B. Chilukuri, R. N. McDougald Jr, M. M. Ghimire, V. N. Nesterov, U. Mazur, M. A. Omary and K. W. Hipps, *J. Phys. Chem. C*, 2015, **119**, 24844–24858.
- 48 Q. Li, T.-Y. Luo, M. G. Taylor, S. Wang, X. Zhu, Y. Song, G. Mpourmpakis, N. L. Rosi and R. Jin, *Sci. Adv.*, 2017, **3**, e1603193.
- 49 A. C. Tsipis, *Coord. Chem. Rev.*, 2017, **345**, 229–262.
- 50 *The Chemical Bond*, ed. G. Frenking and S. Shaik, Wiley-VCH Verlag GmbH & Co. KGaA, Weinheim, Germany, 2014.
- 51 H. Schmidbaur and H. G. Raubenheimer, *Angew. Chem., Int. Ed.*, 2020, **59**, 14748–14771.
- 52 J. Joy, D. Danovich, M. Kaupp and S. Shaik, *J. Am. Chem. Soc.*, 2020, **142**, 12277–12287.
- 53 H. Schmidbaur and A. Schier, *Chem. Soc. Rev.*, 2008, **37**, 1931–1951.
- 54 F. Muniz-Miranda, M. C. Menziani and A. Pedone, *J. Phys. Chem. C*, 2015, **119**, 10766–10775.
- 55 R.-W. Huang, Y.-S. Wei, X.-Y. Dong, X.-H. Wu, C.-X. Du, S.-Q. Zang and T. C. W. Mak, *Nat. Chem.*, 2017, **9**, 689–697.
- 56 W.-P. To, G. S. M. Tong, W. Lu, C. Ma, J. Liu, A. L.-F. Chow and C.-M. Che, *Angew. Chem., Int. Ed.*, 2012, **51**, 2654–2657.
- 57 L.-R. Xing, Z. Lu, M. Li, J. Zheng and D. Li, *J. Phys. Chem. Lett.*, 2020, **11**, 2067–2073.
- 58 M. A. Rawashdeh-Omary, M. A. Omary and H. H. Patterson, *J. Am. Chem. Soc.*, 2000, **122**, 10371–10380.
- 59 E. Ben-Naim and P. L. Krapivsky, *Phys. Rev. Lett.*, 2009, **102**, 190602.
- 60 (a) G. M. Sheldrick, *Acta Crystallogr., Sect. A: Found. Adv.*, 2015, **71**, 3–8; (b) M. C. Burla, R. Caliandro, M. Camalli, B. Carrozzini, G. L. Casciarano, L. De Caro, C. Giacovazzo, G. Polidori and R. Spagna, *J. Appl. Crystallogr.*, 2005, **38**, 381–388; (c) O. V. Dolomanov, L. J. Bourhis, R. J. Gildea, J. A. K. Howard and H. Puschmann, *J. Appl. Crystallogr.*, 2009, **42**, 339–341; (d) G. M. Sheldrick, *Acta Crystallogr., Sect. C: Struct. Chem.*, 2015, **71**, 3–8.